Biogeosciences, 15, 5715–5731, 2018
https://doi.org/10.5194/bg-15-5715-2018

Biogeosciences Open Access EGU

On the formation of hydrothermal vents and cold seeps in the Guaymas Basin, Gulf of California

Sonja Geilert[1], Christian Hensen[1], Mark Schmidt[1], Volker Liebetrau[1], Florian Scholz[1], Mechthild Doll[2], Longhui Deng[3], Annika Fiskal[3], Mark A. Lever[3], Chih-Chieh Su[4], Stefan Schloemer[5], Sudipta Sarkar[6], Volker Thiel[7], and Christian Berndt[1]

[1]GEOMAR Helmholtz Centre for Ocean Research Kiel, Wischhofstraße 1–3, 24148 Kiel, Germany
[2]Faculty of Geosciences, University of Bremen, Klagenfurter-Straße 4, 28359 Bremen, Germany
[3]Department of Environmental Systems Science, ETH Zurich, Universitätstrasse 16, 8092 Zurich, Switzerland
[4]Institute of Oceanography, National Taiwan University, No. 1, Sec. 4, Roosevelt Road, Taipei 106, Taiwan
[5]Federal Institute for Geosciences and Natural Resources, Stilleweg 2, 30655 Hannover, Germany
[6]Department of Earth and Climate Science, Indian Institute of Science Education and Research Pune, Dr. Homi Bhabha Road, Maharashtra-411008, India
[7]Geobiology, Geoscience Centre, University of Göttingen, Goldschmidtstr. 3, 37077 Göttingen, Germany

Correspondence: Sonja Geilert (sgeilert@geomar.de)

Received: 8 January 2018 – Discussion started: 6 February 2018
Revised: 4 September 2018 – Accepted: 5 September 2018 – Published: 27 September 2018

Abstract. Magmatic sill intrusions into organic-rich sediments cause the release of thermogenic CH_4 and CO_2. Pore fluids from the Guaymas Basin (Gulf of California), a sedimentary basin with recent magmatic activity, were investigated to constrain the link between sill intrusions and fluid seepage as well as the timing of sill-induced hydrothermal activity. Sampling sites were close to a hydrothermal vent field at the northern rift axis and at cold seeps located up to 30 km away from the rift. Pore fluids close to the active hydrothermal vent field showed a slight imprint by hydrothermal fluids and indicated a shallow circulation system transporting seawater to the hydrothermal catchment area. Geochemical data of pore fluids at cold seeps showed a mainly ambient diagenetic fluid composition without any imprint related to high temperature processes at greater depth. Seep communities at the seafloor were mainly sustained by microbial methane, which rose along pathways formed earlier by hydrothermal activity, driving the anaerobic oxidation of methane (AOM) and the formation of authigenic carbonates.

Overall, our data from the cold seep sites suggest that at present, sill-induced hydrothermalism is not active away from the ridge axis, and the vigorous venting of hydrothermal fluids is restricted to the ridge axis. Using the sediment thickness above extinct conduits and carbonate dating, we calculated that deep fluid and thermogenic gas flow ceased 28 to 7 kyr ago. These findings imply a short lifetime of hydrothermal systems, limiting the time of unhindered carbon release as suggested in previous modeling studies. Consequently, activation and deactivation mechanisms of these systems need to be better constrained for the use in climate modeling approaches.

1 Introduction

Abrupt climate change events in Earth's history have been partly related to the injection of large amounts of greenhouse gases into the atmosphere (e.g., Svensen et al., 2004; Gutjahr et al., 2017). Among the most prominent of these events was the Paleocene–Eocene Thermal Maximum (PETM) during which the Earth's atmosphere warmed by about 8 °C in less than 10 000 years (Zachos et al., 2003). The PETM was possibly triggered by the emission of about 2000 Gt of carbon (Dickens, 2003; Zachos et al., 2003). The processes discussed regarding the release of these large amounts of carbon in a relatively short time are gas hydrate dissociation, volcanic eruptions as well as igneous intrusions into organic-rich sediments, triggering the release of carbon during con-

tact metamorphism (Svensen et al., 2004; Aarnes et al., 2010; Gutjahr et al., 2017).

The Guaymas Basin in the Gulf of California is considered one of the few key sites to study carbon release in a rift basin exposed to high sedimentation rates. A newly discovered vent field in the Guaymas Basin, which releases large amounts of CH_4 and CO_2 up to several hundreds of meters into the water column (Berndt et al., 2016), stimulated the discussion on the climate potential of magmatic intrusions into organic-rich sediments (e.g., Svensen et al., 2004).

The Gulf of California is located between the Mexican mainland and the Baja California peninsula, north of the East Pacific Rise (EPR; Fig. 1). The spreading regime at EPR continues into the Gulf of California and changes from a mature, open-ocean type to an early opening continental rifting environment with spreading rates of about 6 cm yr^{-1} (Curray and Moore, 1982). Its spreading axis consists of two graben systems (northern and southern troughs) offset by a transform fault (Fig. 1). The Guaymas Basin, which is about 240 km long, is around 60 km wide, reaches water depths of up to 2000 m, and is known as a region of vigorous hydrothermal activity (e.g., Curray and Moore, 1982; Gieskes et al., 1982; Von Damm et al., 1985). Hydrothermal activity in the Guaymas Basin was first reported in the southern trough (e.g., Lupton, 1979; Gieskes et al., 1982; Campbell and Gieskes, 1984; Von Damm et al., 1985). Here, fluids emanate partly from black-smoker-type vents at temperatures of up to 315 °C (Von Damm et al., 1985). The rifting environment in the Guaymas Basin shows a high sediment accumulation rate of up to 0.8–2.5 m kyr^{-1}, resulting in organic-rich sedimentary deposits of several hundreds of meters in thickness (e.g., Calvert, 1966; DeMaster, 1981; Berndt et al., 2016). The high sedimentation rate is caused by high biological productivity in the water column and an influx of terrigenous matter from the Mexican mainland (Calvert, 1966). Sills and dikes intruding into the sediment cover have a substantial impact on the distribution of heat flow, other environmental conditions, and thus early diagenetic processes within the basin (Biddle et al., 2012; Einsele et al., 1980; Kastner, 1982; Kastner and Siever, 1983; Simoneit et al., 1992; Lizarralde et al., 2010; Teske et al., 2014).

Magmatic intrusions and cold seeps at the seafloor were observed up to 50 km away from the rift axis, and a recently active magmatic process triggering the alteration of organic-rich sediments and releasing thermogenic CH_4 and CO_2 was proposed by Lizarralde et al. (2010). These authors attributed elevated CH_4 concentrations and temperature anomalies in the water column to active thermogenic CH_4 production driven by contact metamorphism. According to Lizarralde et al. (2010) ongoing off-axis hydrothermal activity may cause a maximum carbon flux of 240 kt C yr^{-1} through the seafloor into the ocean and potentially into the atmosphere. However, modeling studies investigating the lifetime of such sill-induced hydrothermalism show that initial CH_4 and CO_2 release is intense and vigorous but can decline just as quickly (< 10 kyr) (Bani-Hassan, 2012; Iyer et al., 2017).

During the expedition SO241 by RV SONNE in June/ July 2015 a new hydrothermal vent field was discovered at the flank of the northern trough (Fig. 1; Berndt et al., 2016). The discovered mound rises up to 100 m above the seafloor and predominant black-smoker-type vents suggest similar end-member temperatures and geochemical composition found at the southern trough (Von Damm et al., 1985; Von Damm, 1990; Berndt et al., 2016). The hydrothermal vent system emits methane-rich fluids with a helium isotope signature indicative of fluids in contact with mid-ocean ridge basalt (Berndt et al., 2016). On this cruise, we sampled this recently discovered hydrothermal vent field and some of the off-axis seeps above sill intrusions described by Lizarralde et al. (2010). The aim of this study was to investigate the fluid and gas compositions of the off-axis seeps in order to identify the influence of sill intrusions on fluid circulation, gas composition, and the timing of hydrothermal activity. The overall motivation was thus to explore the regional and temporal extent of hydrothermal activity in the area and to provide better constraints on carbon release from sedimented ridge systems.

2 Materials and methods

2.1 Sampling devices and strategy

During the RV SONNE expedition SO241, seven sites across the central graben of the Guaymas basin were investigated (Fig. 1). Site-specific sampling and data recording were performed using (1) a video-guided multi-corer (MUC), (2) a gravity corer (GC), (3) temperature loggers attached to a GC or sediment probe, (4) a video-guided VCTD/Rosette water sampler, and (5) a video-guided hydraulic grab (VgHG). Sites were selected according to published data on the locations of seeps (Lizarralde et al., 2010) and seismic data acquired during the cruise (see below).

2.1.1 Seismic data recording

Seismic data were collected using a Geometrics GeoEel Streamer of 150 and 183.5 m length and 96 and 112 channels, respectively. Two generator-injector guns in harmonic mode (105/105 cubic inch) served as the seismic source. Processing included navigation processing (1.5625 m crooked line binning), 20, 45, 250, and 400 Hz frequency filtering, and post-stack Stolt migration with water velocity yielding an approximately 2 m horizontal and 5 m vertical resolution close to the seafloor.

2.1.2 Sediment and pore fluid sampling

At seepage and vent sites, the video-guided MUC was used to discover recent fluid release, which was indicated by typical chemosynthetic biological communities at the seafloor

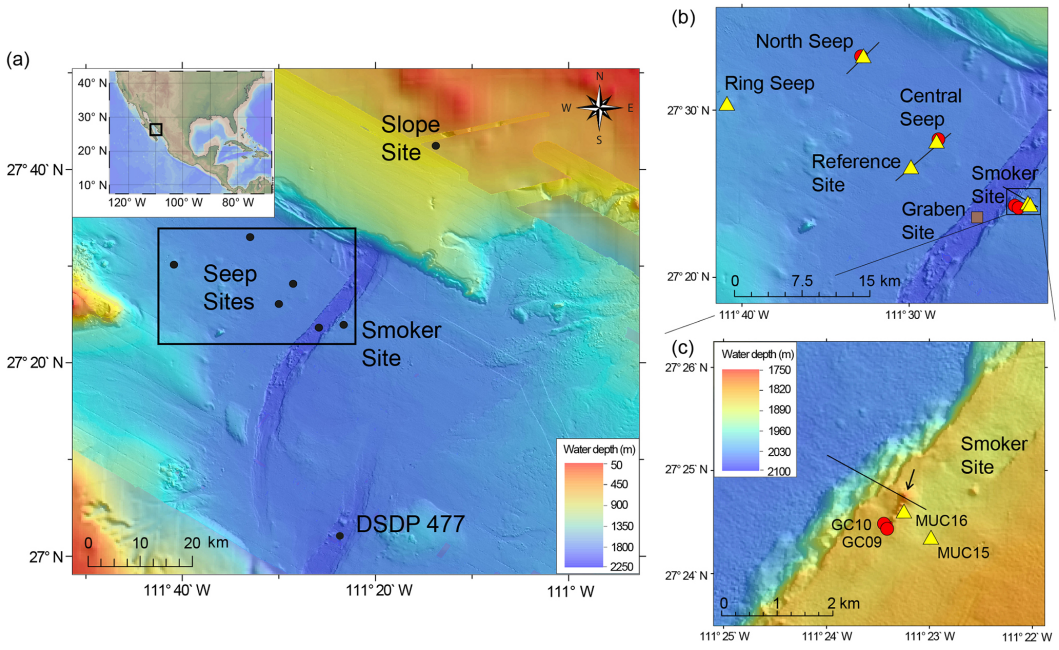

Figure 1. Sample locations in the Guaymas Basin, Gulf of California studied during RV SONNE expedition SO241. **(a)** Overview of stations (Seep sites, Smoker Site, and Slope Site). Black square indicates enlarged area in **(b)**. Site DSDP 477 in the southern trough is shown for comparison. **(b)** Enlargement of the sampling locations. Red circles refer to GC employments and yellow triangles to MUCs. Brown square at Graben Site refers to water-column sampling and temperature measurements. Black lines refer to seismic profiles displayed in Fig. 2. **(c)** Enlargement of the Smoker Site sampling locations. Note the different scale compared to **(a)** and **(b)**. Black arrow refers to the location of the hydrothermal mound described in Berndt et al. (2016).

(microbial mats, bivalves, etc.; Sahling et al., 2002). However, small-scale, patchy distributions of active seepage spots and the visibility of authigenic carbonate concretions made it difficult to select the best locations for coring. Hence, the comparison of results from different seeps might be biased in this regard, as not all seepage areas could be sampled at their most active places. GC deployments were typically performed at sites initially investigated with the MUC video system or at the center of suspected seeps (based on bathymetry and seismic data).

In total, we present pore fluid and gas data collected at the seepage sites North (GC01, MUC11), Central (GC03, GC13, GC15, MUC04), and Ring (MUC05), one reference site (see Reference Site below; GC04, MUC02), and the hydrothermal vent field (Smoker Site; GC09, GC10, MUC15, MUC16). The Reference Site that did not show active seepage or faults indicated by seismic data was chosen to obtain geochemical background values. In addition, the slope towards the Mexican mainland was sampled as well (Slope Site; GC07) (Fig. 1, Table 1). Immediately after core retrieval, GCs were cut, split, and subsampled. Samples were transferred into a cold lab at 4 °C and processed within 1 or 2 h. Pore fluids were obtained by pressure filtration (e.g., Jahnke et al., 1982). After MUC retrieval, bottom water was sampled and immediately filtered for further analyses. The sediment was transferred into a cold lab and sampling was executed in an argon-flushed glove bag. Pore fluids were retrieved by centrifugation and subsequent filtration using 0.2 µm cellulose acetate membrane filters (e.g., Jahnke et al., 1982). Sediment samples (2 cm^3) for hydrocarbon analyses were taken using cut-off 3 mL syringes. All hydrocarbon samples were taken immediately after sediment surfaces were exposed after core cutting or sectioning, ensuring minimal disturbance to sediment surfaces prior to sampling and transferred to vials containing concentrated NaCl solution (as seen in Sommer et al., 2009). MUCs were extruded and sampled from the top. GCs were sampled at the bottom ends of 1-m core sections, either at the core catcher or at freshly cut section ends. In some cases additional samples were taken from within GC core sections by cutting the core liner with an oscillating saw and inserting cut-off syringes into the sides of core sections.

2.1.3 Sub-seafloor temperature measurements

Temperature gradients and thermal conductivity were measured at the North Seep, Central Seep, Reference Site, and Smoker Site as well as along a transect across the newly discovered hydrothermal vent field and the rift valley (Graben Site). Miniaturized temperature loggers (MTL) were attached to GCs or to a 5 m long sediment lance at a sampling rate of 1 measurement per second. The absolute accuracy of these temperature measurements was about 0.1 K and the

Table 1. Station list and site names of GCs and MUCs taken in the Guaymas Basin with corresponding water depths. Heat flow and temperature gradient data measured either attached to GCs or to a sediment probe.

Site	Site name	Latitude (N)	Longitude (W)	Water depth (m)	Temp. gradient ($K\,m^{-1}$)	Heat flow ($mW\,m^{-2}$)	SR ($m\,kyr^{-1}$)	MAR ($g\,cm^{-2}\,yr^{-1}$)
GCs								
St.07-GC01	North Seep	27°33.301′	111°32.882′	1845	0.14	28	n.d.	n.d.
St.10-GC04	Reference Site	27°26.531′	111°29.928′	1846	0.22	140	n.d.	n.d.
St.09-GC03	Central Seep	27°28.138′	111°28.420′	1837	n.d.	n.d.	n.d.	n.d.
St.09-GC13	Central Seep	27°28.193′	111°28.365′	1838	0.16	113	n.d.	n.d.
St.72-GC15	Central Seep	27°28.178′	111°28.396′	1837	n.d.	n.d.	n.d.	n.d.
St.51-GC09	Smoker Site	27°24.472′	111°23.377′	1840	11	8069	n.d.	n.d.
St.58-GC10	Smoker Site	27°24.478′	111°23.377′	1845	10	6509	n.d.	n.d.
St.47-GC07	Slope Site	27°24.412′	111°13.649′	671	n.d.	n.d.	n.d.	n.d.
MUCs								
St.33-MUC11	North Seep	27°33.301′	111°32.883′	1855	n.d.	n.d.	1.7[a] 3.5[a]	0.05[a] 0.15[a]
St.23-MUC05	Ring Seep	27°30.282′	111°40.770′	1726	n.d.	n.d.	0.5	0.01
St.15-MUC02	Reference Site	27°26.925′	111°29.926′	1845	n.d.	n.d.	2.3	0.04
St.22-MUC04	Central Seep	27°28.165′	111°28.347′	1839	n.d.	n.d.	1.7	0.04
St.65-MUC15	Smoker Site	27°24.342′	111°22.970′	1846	n.d.	n.d.	1.8	0.05
St.66-MUC16	Smoker Site	27°24.577′	111°23.265′	1842	n.d.	n.d.	$2.1^{\prime b}$ 0.4^{+b}	$0.08^{\prime b}$ 0.02^{+b}
HF lance								
St.60a – HF008_P03	Smoker Site	27°24.273′	111°23.396′	1840	4.6	3206	n/a	n/a
St.60a – HF008_P01		27°24.623′	111°23.626′	1834	0.86	599	n/a	n/a
St.60a – HF008_P02		27°24.554′	111°23.512′	1840	2.8	1953	n/a	n/a
St.60a – HF008_P04		27°24.408′	111°23.288′	1849	2039	1427	n/a	n/a
St.60a – HF008_P05		27°24.341′	111°23.177′	1852	1014	710	n/a	n/a
St.60a – HF008_P06		27°24.265′	111°23.082′	1844	0.74	516	n/a	n/a
St.60b – HF008_P07		27°24.193′	111°23.956′	1834	0.8	579	n/a	n/a
St.60b – HF009_P04		27°24.543′	111°23.351′	1837	15	10 835	n/a	n/a
St.60b – HF009_P01		27°24.605′	111°23.317′	1837	0.39	274	n/a	n/a
St.60b – HF009_P02		27°24.552′	111°23.347′	1834	3451	2415	n/a	n/a
St.70 – HF011_P01	Graben Site	27°25.802′	111°25.486′	1870	0.38	262	n/a	n/a
St.70 – HF011_P02		27°25.460′	111°24.946′	2019	0.48	338	n/a	n/a
St.70 – HF011_P03		27°25.955′	111°24.493′	2046	0.43	302	n/a	n/a
St.70 – HF011_P04		27°25.837′	111°24.951′	2025	0.46	320	n/a	n/a
Authigenic carbonate								
St.56-VgHG-4	Central Seep	27°28.181′	111°28.379′	1843	n/a	n/a	n/a	n/a

Abbreviations: SR, Sedimentation Rate; MAR, Mass Accumulation Rate; n.d. not determined; n/a not applicable. [a] Sedimentation and mass accumulation rates at Station 33 of the 0–13 and 13–18 cm layers, respectively. [b] Sedimentation and mass accumulation rates at Station 66 of the 0–7 and 7–17 cm layers, respectively.

temperature resolution was 0.001 K (Pfender and Villinger, 2002).

Thermal conductivity was measured on recovered core material in close vicinity to the MTLs using the KD2 Pro Needle Probe instrument. For temperature measurements obtained by a lance, a constant thermal conductivity of $0.7\,W\,m^{-1}\,K$ was assumed. Data processing was done according to Hartmann and Villinger (2002).

2.1.4 Water column sampling

Water samples were taken by using a Niskin water sampler (Rosette System), equipped with a video camera designed for near-seafloor sampling (Schmidt et al., 2015) in order to study water column chemistry (i.e., dissolved CH_4) and oceanographic parameters (i.e., temperature, salinity, turbidity). Eight water sampling locations were chosen in the vicinity of MUC and GC stations and were termed the North Seep (VCTD03), Central Seep (VCTD02), Ring Seep (VCTD01), Graben Site (CTD01; no video-guided sampling), Smoker Site (VCTD06 and 10), and Slope Site (VCTD07). The (V)CTDs were either used in a towed mode (VCTD03, 06, 09, 10) or in station (CTD01; VCTD01, 02, 07) keeping hydrocast mode. The water depth was controlled based on pressure readings, altitude sensors (< 50 m distance to bottom), and online video observation (1–2 m above the seafloor).

2.1.5 Authigenic carbonate sampling

At the Central Seep a block (approx. $1 \times 0.5 \times 0.3$ m) was recovered using a video-guided hydraulic grab (VgHG, GEOMAR) in 1843 m water depth from the surface of a typical cold seep environment (close to high abundance of tube worms) . The block consisted mainly of a solidified carbonate matrix covered by a whitish carbonate rim and was characterized by coarse open pore space in the mm to cm scale (see Supplement Fig. S1).

2.2 Sample treatment and analytical procedures

Pore fluids were analyzed onboard for total dissolved sulfide (TH_2S) and NH_4 directly after recovery by photometry using standard methods described in Grasshoff et al. (2002). Prior to NH_4 measurements, pore fluids containing dissolved sulfide were treated with argon to prevent biased NH_4 measurements. Total alkalinity (TA) was determined by titration immediately after pore-water separation using 0.02 M HCl (Ivanenkov and Lyakhin, 1978). Shore-based analyses of the remaining acidified pore water included dissolved anions (SO_4, Cl) and cations (Li, Mg) using ion chromatography (IC, METROHM 761 Compact, conductivity mode) and inductively coupled plasma optical emission spectrometry (ICP-OES, VARIAN 720-ES), respectively. All chemical analyses were tested for accuracy and reproducibility using the IAPSO salinity standard (Gieskes et al., 1991).

Strontium isotope ratios were analyzed by thermal ionization mass spectrometry (TIMS, Triton, ThermoFisher Scientific). The samples were chemically separated via cation exchange chromatography using the SrSpec resin (Eichrom). The isotope ratios were normalized to the NIST SRM 987 value of 0.710248 (Howarth and McArthur, 2004), which reached a precision of ± 0.000015 (2 sd, $n = 12$). Potential influences of ^{87}Rb interferences on ^{87}Sr / ^{86}Sr isotope ratios were eliminated by combining the highly selective Sr-Spec resin and Rb/Sr-discriminating TIMS preheating procedures with the static mode measurement of ^{85}Rb simultaneously with the Sr masses 84, 86, 87, and 88 for optional Rb/Sr corrections (not required in this study).

Water samples taken from Niskin bottles were transferred into 100 mL glass vials with a helium headspace of 5 mL and poisoned with 50 µL of saturated mercury chloride solution.

The hydrocarbon composition of headspace gases was determined using a CE 8000 TOP gas chromatograph equipped with a 30 m capillary column (Restek Q-PLOT, 0.32 mm) and a flame ionization detector (FID). Replicate measurements yielded a precision of < 3 % (2 sd).

Stable carbon isotopes of methane were measured using a continuous-flow isotope-ratio mass spectrometer (cf-IRMS). A Thermo TRACE gas chromatograph was used to separate the light hydrocarbon gases by injecting up to 1 mL headspace gas on a ShinCarbon ST100/120 packed gas chromatography column. The separated gases were combusted and corresponding δ^{13}C values were determined using a Thermo MAT 253 mass spectrometer. The reproducibility of δ^{13}C measurements was ± 0.3 ‰ (2 sd), based on repeated measurements of the reference standard Vienna Pee Dee Belemnite (VPDB).

Stable hydrogen isotope compositions of methane were analyzed by separating methane from other gases by online gas chromatography (Thermo Trace GC, isotherm at 30 °C; 30 m RT-Q-Bond column, 0.25 mm ID, film thickness 8 µm). Methane-H was reduced to dihydrogen at 1420 °C prior to stable isotope analysis using a coupled MAT 253 mass spectrometer (Thermo). Data are reported in per mil relative to Standard Mean Ocean Water (SMOW). The precision of δD-CH_4 measurements was ± 3 ‰ (2 sd).

^{210}Pb (46.52 keV) and ^{214}Pb (351.99 keV) were simultaneously measured on freeze dried sediments by two HPGe gamma spectrometry systems (ORTEC GMX-120265 and GWL-100230), each interfaced to a digital gamma-ray spectrometer (DSPecPlus™). The efficiency calibration of the gamma detectors were calibrated using IAEA reference materials (for GMX-type detector – 327A, 444 spiked soil, CU-2006-03 spiked soil, RGTh and RGU for sample weight at 100 g; for well-type detector – IAEA-RGTh and RGU from 0.5 to 3.5 g), coupled with an in-house secondary standard ("Rock-falling Mountain soils", Radiation Monitoring Center of the Atomic Energy Council, Taiwan) for various masses (Lee et al., 2004; Huh et al., 2006). ^{214}Pb was used as an index of ^{226}Ra (supported ^{210}Pb) whose activity concentration was subtracted from the total ^{210}Pb to obtain the excess ^{210}Pb ($^{210}Pb_{ex}$). The activities of radionuclides were decay-corrected to the date of sample collection. All radionuclide data were calculated on salt-free dry weight basis.

A representative sample of the authigenic carbonate (cm-scale) was broken from the upper surface of the block, gently cleaned from loosely bound sediment and organic remains, and dried at 20 °C for 12 h. Two different subsamples were prepared by drilling material with a handheld mm-sized mini-drill from the outer rim (whitish coating, lab code: 470-15) and the related inner core (dark matrix, lab code: 472-15).

Prior to aliquot procedures both subsamples were finely ground in an agate mortar providing homogeneous aliquots of suitable grain size for the mineral identification by X-ray diffractometry (XRD) (Philips X-ray diffractometer PW 1710 in monochromatic CuKα mode between 2 and 70 2θ, incident angle, for details see Supplement). Subsamples were analyzed for δ^{18}O and δ^{13}C by stable isotope-ratio mass spectrometry (SIRMS) and U-Th geochronology by multi-collector inductively coupled plasma-mass spectrometry (MC-ICP-MS) on a parallel leachate/sequential dissolution approach for single and isochron ages (for method see Supplement). Furthermore, ^{87}Sr / ^{86}Sr isotope signatures for aliquots of the individual U-Th solutions by thermal ionization mass spectrometry (TIMS, for method details please refer to pore-water Sr isotope analyses) were determined. Lipid extracts for biomarker analyses were determined as well.

From each homogenized carbonate powder sample, an aliquot of 10 mg was separated for carbon $\delta^{13}C$ and oxygen $\delta^{18}O$ stable isotope analysis. A fraction of this (approximately 1 mg) was dissolved by water-free phosphoric acid at 73 °C in a "Carbo-Kiel" (Thermo Fischer Scientific Inc.) online carbonate preparation line and measured for carbon and oxygen stable isotope ratios with a MAT 253 mass spectrometer (Thermo-Fischer Inc.). The $\delta^{13}C$ and $\delta^{18}O$ values were calculated as deviations from the laboratory standard, referred to the PDB scale, and reported in ‰ relative to V-PDB. The external reproducibility was checked by replicate analyses of laboratory standards as being better than ±0.04 ‰ for $\delta^{13}C$ and ±0.1 ‰ for $\delta^{18}O$ (1 sd, $n = 7$) for this sample set. However, the single measurement uncertainties were significantly better and the resulting 2 sd ($n = 3$) for both main samples are given in the Supplement Table S5.

Biomarkers were extracted from 4 g of a powdered sample and were then sequentially extracted with dichloromethane (DCM)/methanol (3/1, v/v), DCM, and n-hexane (ultrasonication, 20 min). The combined extracts were dried, derivatized using a BSTFA/trimethylchlorosilane mixture (95/5, v/v; 1 h; 40 °C), and analyzed by coupled gas chromatography–mass spectrometry (GC-MS; Hinrichs et al., 2000). GC-MS analyses were carried out with a Thermo Fisher Trace 1310 GC coupled with a Quantum XLS Ultra MS. The instrument was equipped with a Phenomenex Zebron ZB 5MS capillary column (30 m, 0.1 µm film thickness, inner diameter 0.25 mm). Fractions were injected without splits at 270 °C. The carrier gas was He (1.5 mL min^{-1}). The GC oven temperature was ramped from 80 °C (1 min) to 310 °C at 5 °C min^{-1} and held for 20 min. Electron ionization mass spectra were recorded at 70 eV.

3 Results

3.1 Subsurface structure and evidence for sill-related fluid mobilization

Seismic profiles showed a wide range of sediment deformation (Fig. 2). Seismic amplitude blanking along vertical zones below the seafloor indicated the flow of gaseous pore fluids at the North, Central, and Ring seeps (Fig. 2). Underneath these locations sediments were deformed, probably due to sediment mobilization associated with hydrothermal activity in response to sill intrusion. In contrast the Reference Site sediments showed a more or less continuous succession without vertical disturbance. At the North Seep, a shallow high-amplitude reversed polarity reflector occurred at 50–60 ms. Sill depths were inferred from the seismic profiles at ∼ 500 to 600 m below seafloor (m b.s.f.) for the North Seep and with ∼ 350 to 400 m b.s.f. at the other sites, assuming seismic interval velocities of 1600 to 2000 m s^{-1}. Seismic images suggest that massive disturbance of sediments and vertical pipe structures are related to channeled fluid and/or gas advection caused by sill intrusions (Fig. 2). Faults are indicated that may serve as fluid pathways above potential sill intrusions. A closer inspection of the seismic reflectors at the Central Seep (Fig. 2c) shows onlap onto a doming structure. On the NW flank of the dome, the deepest onlap occurs at 60 ms or 48 m b.s.f. (assuming 1600 m s^{-1} sediment interval velocity), whereas on the SE flank, the shallowest onlap occurs at 15 ms or 12 m b.s.f.

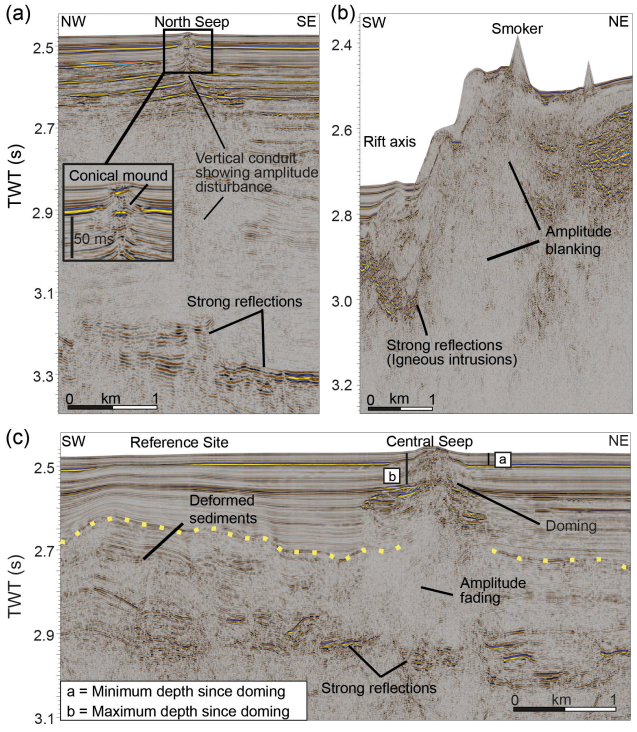

Figure 2. Seismic profiles of the North Seep **(a)**, Smoker Site **(b)** as well as of the Central Seep and Reference Site **(c)**. Seismic section showing doming above the Central Seep. There are different phases of onlap starting about 60 ms (maximum deposition) until about 15 ms (minimum deposition) or 48 and 12 m b.s.f., respectively, assuming a sediment interval velocity of 1600 m s^{-1}.

3.2 Temperature measurements

Heat flow and temperature gradients were measured at the North and Central seeps, Reference Site, and Smoker Site (attached to GCs) as well as in transects along the hydrothermal ridge and rift axis (attached to a temperature lance; Figs. 3 and S2, Table 1). Temperature gradients are shown in Fig. S2. The highest heat flows occurred close to the Smoker Site and ranged from 599 to 10 835 mW m^{-2}. Temperature gradients were also highest at the Smoker Site (∼ 15 K m^{-1}). In contrast, heat flows and temperature gradients in the rift valley close to the rift axis ranged from 262 to 338 mW m^{-2} and 0.4 to 0.5 K m^{-1}, respectively. Generally heat flow values decreased with increasing distance to the rift axis with 140 mW m^{-2} at the Reference Site, 113 mW m^{-2} at the Cen-

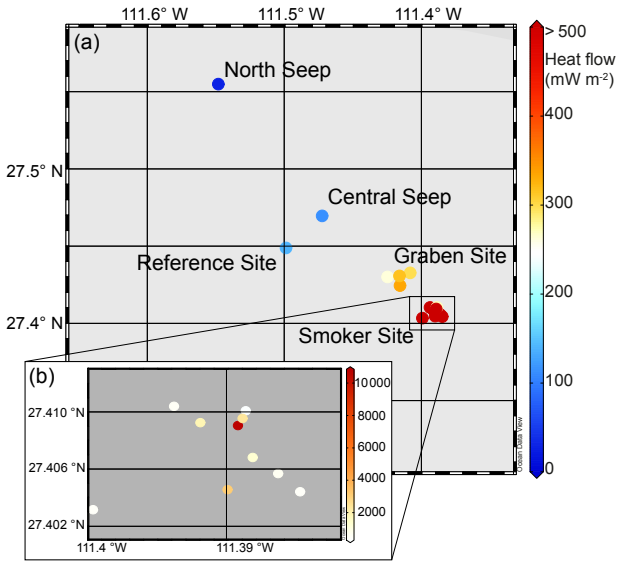

Figure 3. (a) Heat flow in the vicinity of the northern trough. Note the different heat flow scale in the enlarged area of the Smoker Site **(b)**.

tral Seep, and 28 mW m^{-2} at the North Seep. Temperature gradients were 0.22 K m^{-1} at the Reference Site, 0.16 K m^{-1} at the Central Site and 0.14 K m^{-1} at the North Site.

3.3 Sediment characteristics and sedimentation rates

The sediments were mainly composed of organic-rich diatomaceous clay, consistent with earlier analyses (e.g., Kastner, 1982). At the North Seep, the sediments were composed of homogeneous diatomaceous clay containing rare shell fragments and carbonate concretions. Gas hydrates were discovered at 2.5 m b.s.f. Authigenic carbonates were exposed at the seafloor. At the Ring Seep, SW of the North Seep, sediments were predominantly composed of diatomaceous clay. At the Central Seep, located between the North Seep and Smoker Site, sediments were composed of homogeneous diatomaceous clay intercalated with whitish layers and shell fragments occurring in the shallow sediment ($\leq$ 70 cm). Again, authigenic carbonates were observed on the seafloor. At the Smoker Site, ca. 500 m SE of the hydrothermal vent field, surface sediments were likewise composed of diatomaceous clay with light and dark greyish banding. Traces of bioturbation were visible in the upper 4 m. At this depth, a sharp contact defined the transition to the underlying hydrothermal deposits, which were composed of millimeter-to-centimeter-sized black to grey Fe-rich sulfides (for a detailed description see Berndt et al., 2016). Within the hydrothermal deposits, brownish to grey clay lenses appeared. At the Slope Site, sediments were laminated in the millimeter to centimeter range. The sediment was dominated by diatomaceous clay that contained a few ash lenses.

The sedimentation rates ranged from 0.4 m kyr^{-1} at the Smoker Site to 3.5 m kyr^{-1} at the North Seep, based on radionuclide measurements (Table 1). Sedimentation rates at all other sites were about 2 m kyr^{-1}.

3.4 Pore water geochemistry

All pore-water data and isotope measurements of $^{87}Sr / ^{86}Sr$ are listed in Tables S1 and S2. Pore water profiles of TA, TH_2S, SO_4, CH_4, NH_4, Cl, Mg, and Li are shown in Fig. 4a (GCs) and b (MUCs).

Pore water constituents plotted in Fig. 4 were selected to characterize variations in organic matter diagenesis, the anaerobic oxidation of methane (AOM), and potential water–rock interactions related to subsurface hydrothermal activity. In general, methane concentrations were elevated at the seep locations and at the slope, thus enhancing AOM. TA and TH_2S increased with depth for the North Seep, Central Seep (only MUC04), and Slope Site, while SO_4 was decreasing. AOM depths could only be inferred for the North Seep with $\sim$ 160 cm and the Slope Site with $\sim$ 300 cm. NH_4 was only slightly increasing with depth; higher NH_4-levels were only found at the Slope Site (Fig. 4). Concentrations of Cl, Mg, and Li did not show significant variations from seawater in shallow sediment depths (MUCs). At greater depths (GCs) some deviations from seawater concentration occurred at the North Seep, Smoker Site, and Slope Site. At the North Seep, Mg showed a minor offset at $\sim$ 150 cm depth, while at the Smoker Site Mg concentrations increased continuously. In GC09 at the Smoker Site, Li concentrations increased and Mg concentrations decreased abruptly at a depth of $\sim$ 400 cm. At the Slope Site, Mg increased slightly below 400 cm sediment depth while Li showed a small decrease above 400 cm.

Sr concentrations and isotopes are plotted in Fig. 5. Sr concentrations showed predominantly modern seawater values, except at the North Seep where they strongly decreased. The $^{87}Sr / ^{86}Sr$ isotope ratios also showed predominantly seawater values (0.709176; Howarth and McArthur, 2004), except for the Smoker Site, where the isotope ratios decreased strongly below the transition between hemipelagic sediments and hydrothermal deposits (Fig. 5). The North and Ring seeps as well as the Smoker Site (GC10) showed slight decreases in $^{87}Sr / ^{86}Sr$. The ratios showed a similar depletion to those from the hydrothermal plume (Berndt et al., 2016).

3.5 Hydrocarbon gases, carbon, and hydrogen isotope data

Concentrations of dissolved hydrocarbons and $\delta^{13}C_{CH_4}$, $\delta^{13}C_{C_2H_6}$, and δD_{CH_4} data are reported in Table S3. Overall, our pore fluid data showed a large variability in $CH_4 / (C_2H_6 + C_3H_8)$, with ratios between 100 and 10 000 and $\delta^{13}C_{CH_4}$ between -26.5 ‰ and -88.2 ‰. Gas hydrate $\delta^{13}C_{CH_4}$ ranged from -57.9 ‰ to -58.9 ‰. The $\delta^{13}C_{C_2H_6}$

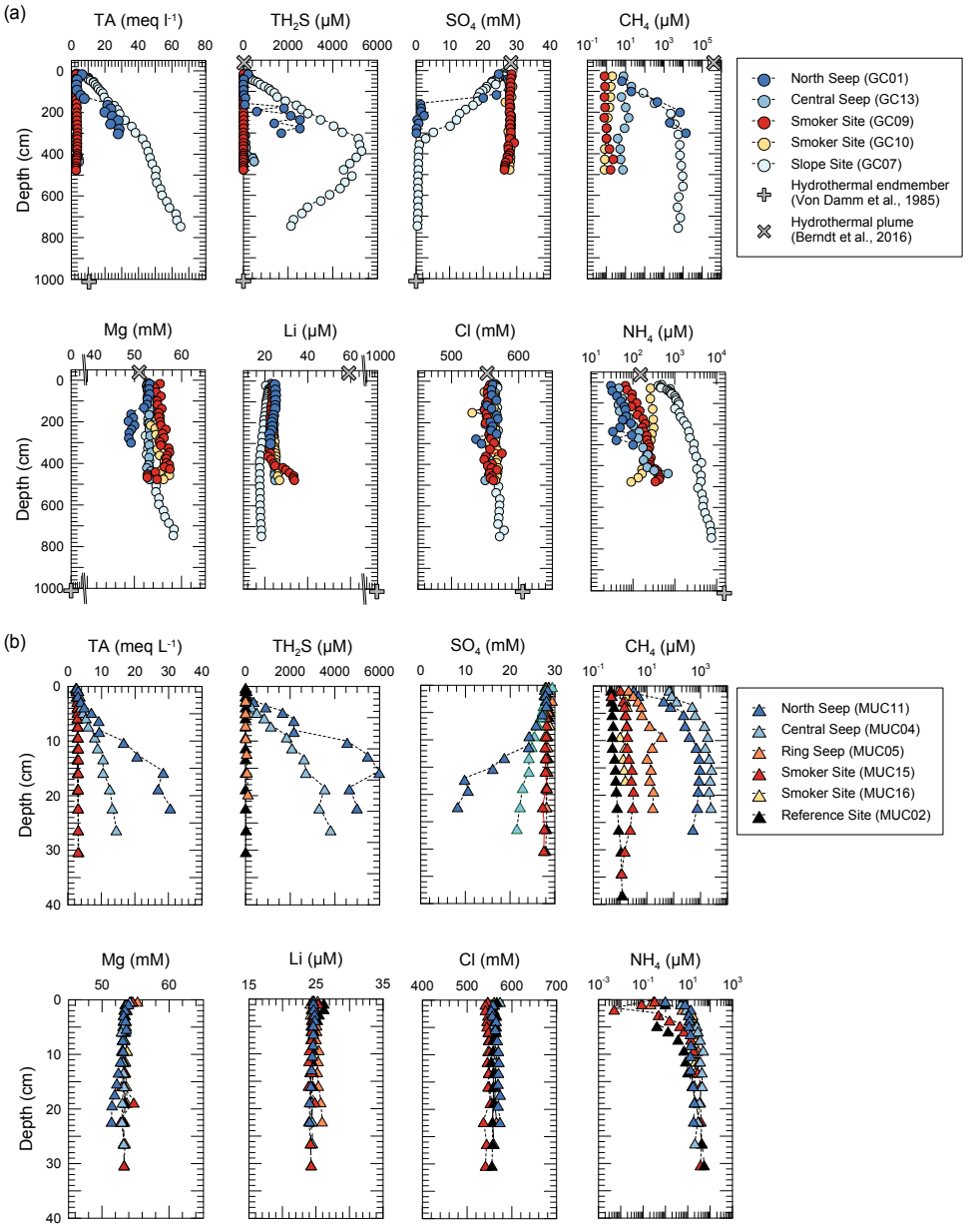

Figure 4. Pore water profiles of GCs **(a)** and MUCs **(b)**. For the Central Seep, GC13 is shown here as an example, and geochemical data of the remaining cores (GC03, 15) can be found in Table S1. Endmember composition of hydrothermal solutions from Von Damm et al. (1985) and hydrothermal plume geochemical composition from Berndt et al. (2016) are shown in **(a)** for comparison.

values ranged between −26.1 ‰ and −38.3 ‰ for the North Seep and −29.6 ‰ and −37.7 ‰ for the Central Seep. The δD_{CH_4} values at both seeps ranged between −97 ‰ and −196 ‰, between −196 ‰ and −198 ‰ for the gas hydrates, between −192 ‰ and −196 ‰ for the Slope Site, and between −98 ‰ and −113 ‰ for the hydrothermal plume (VCTD09).

3.6 Water column data

Water column characteristics like temperature, salinity, turbidity, and methane concentrations are shown in Fig. 6 and Table S4. Surface waters in the Guaymas Basin showed warm temperatures of up to 29.5 °C (salinity: 34.5 ‰) close to the Mexican mainland (Slope Site, VCTD07) and up to 24.6 °C (salinity: 34.6 ‰) in the central basin (Central Seep, VCTD02). With depth, temperatures decreased continuously and ranged from 2.8 to 3.0 °C (salinity: 34.6 ‰) close to the

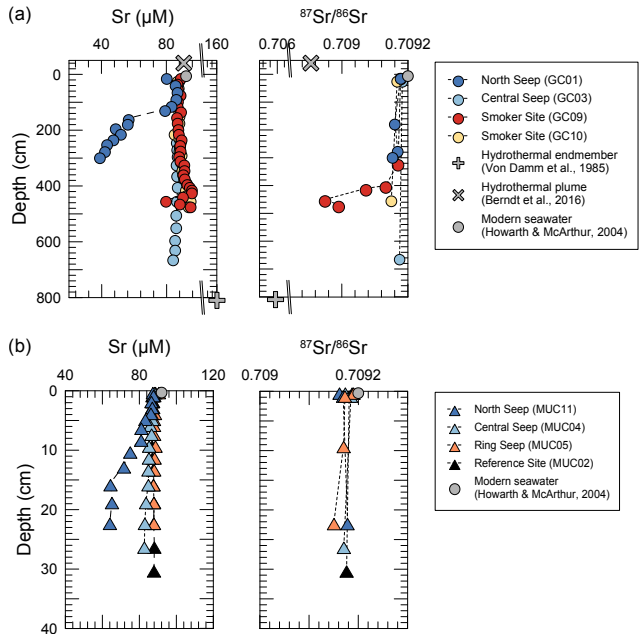

Figure 5. Sr concentrations and ^{87}Sr / ^{86}Sr ratios for GCs **(a)** and MUCs **(b)**. For comparison, data from the hydrothermal plume (Berndt et al., 2016), the hydrothermal endmember (Von Damm et al., 1985), and modern seawater (Howarth and McArthur, 2004) are shown. Note the different x-axis scales for MUC Sr concentration and ^{87}Sr / ^{86}Sr ratios.

seafloor (1600–1800 m). Turbidity values were high in the deep water layer ($\sim$ 1400–1800 m) and indicate a well-mixed deep basin, also shown by relatively homogeneous temperature and salinity data. Only the water column directly above the hydrothermal vent field showed a strongly elevated temperature (28.4 °C) and salinity (35.1 ‰) (Berndt et al., 2016). Methane concentrations were highest close to the hydrothermal vent field (up to 400 µM; VCTD09 from Berndt et al., 2016) but still varied in the deep water column of the basin between 2 and 28.1 nM (Central Seep, VCTD02 and Ring Seep, VCTD01, respectively).

3.7 Authigenic carbonate data

The authigenic carbonate sample (Fig. S1) consisted of 88 to 90 % aragonite and 6 to 12 % calcite (Table S5). By the uncertainty related maximum deviation of Δd104 (<0.01), the XRD spectrum identified calcite with an Mg fraction below 3 %, according to Goldsmith et al. (1961). The bulk outer-rim carbonate had an average carbon isotope signature ($\delta^{13}C_{V\text{-}PDB}$) of -46.6 ± 0.2 ‰ and an oxygen isotope signature ($\delta^{18}O_{V\text{-}PDB}$) of 3.7 ± 0.3 ‰. Inner- core carbonate isotope signatures yielded similar values, with $\delta^{13}C_{V\text{-}PDB}$ of -44.7 ± 0.4 ‰ and $\delta^{18}O_{V\text{-}PDB}$ of 3.6 ± 0.1 ‰ (Table S5). The average outer rim ^{87}Sr / ^{86}Sr ratio was 0.709184 ± 0.000027 and the inner-core ratio was 0.709176 ± 0.000003. The U-Th carbonate dating approach on these authigenic carbonates implied formation ages younger than 240 yrs BP.

Lipid extracts obtained from the seep carbonate 56-VgHG-4 (Central Seep) revealed a strong signal of specific prokaryote-derived biomarkers (Fig. S1). These compounds encompassed isoprenoid lipids derived from archaea, particularly crocetane, 2,6,10,15,19-pentamethylicosane(-icosenes; PMI, PMIΔ), archaeol, and *sn*2-hydroxyarchaeol (see Fig. S1 for structures). In addition, the sample contained a suite of non-isoprenoid 1,2-dialkylglycerolethers (DAGE) of bacterial origin. Typical compounds of planktonic origin, such as sterols, were also present but were low in abundance.

4 Discussion

4.1 Origin of seeping fluids

4.1.1 Smoker Site

The water column above the newly discovered hydrothermal vent field exhibits elevated CH_4 concentrations (up to 400 µM) and pCO_2 data (> 6000 µatm) (Berndt et al., 2016). The range of the measured stable isotope signature of methane ($\delta^{13}C_{CH_4}$ between -39 ‰ and -14.9 ‰) and the helium isotope anomaly (^3He / ^4He ratio of 10.8×10^{-6}) clearly indicate the existence of gas exhalations from thermogenic organic matter degradation with contributions from a mantle source (see Berndt et al., 2016). These northern trough hydrothermal fluids are comparable in their gas geochemistry to the southern trough (Lupton, 1979; Von Damm et al., 1985; Berndt et al., 2016). However, the highest heat flow values of up to 10 835 mW m^{-2} measured in this study are found close to the Smoker Site and are much higher than those observed in earlier studies (maximal 2000 mW m^{-2}, Fisher and Becker, 1991). The high heat flow at the Smoker Site even exceeds the more hydrothermally active southern trough, where heat flow values of 2000 to 9000 mW m^{-2} were measured (Lonsdale and Becker, 1985; Fisher and Becker, 1991). This might indicate that hydrothermal activity at the northern trough is younger and possibly a more recent process compared to the southern trough.

Hydrothermal fluids are typically depleted in Mg and are highly enriched in fluid-mobile elements like Li caused by high-temperature reactions with mafic rocks (here sills) and/or sediments through which they percolate (e.g., Einsele et al., 1980; Gieskes et al., 1982; Kastner, 1982; Von Damm et al., 1985; Lizarralde et al., 2010; Teske et al., 2016). Such compositions were reported from DSDP site 477 (Gieskes et al., 1982) and fluids obtained by Alvin dives (Von Damm et al., 1985) (see Fig. 1 for location of Site DSDP 477). Although strongly diluted, CTD samples from the hydrothermal plume in the northern trough show this trend (Berndt et al., 2016).

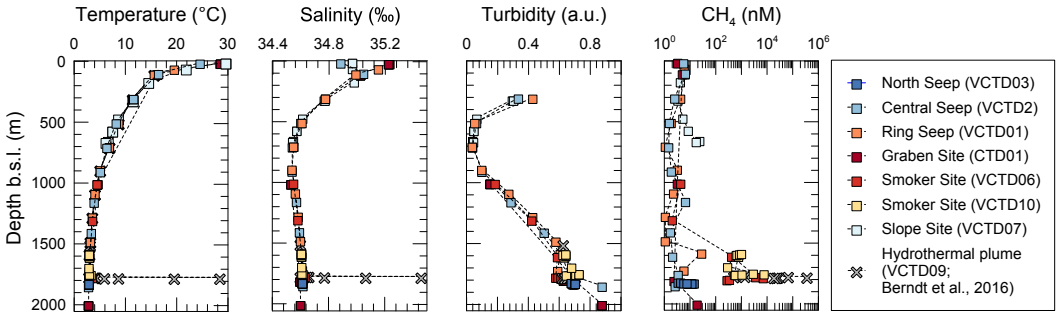

Figure 6. Water column temperature, salinity, turbidity, and methane concentrations. Note that the upper ∼ 300 m below sea level (b.s.l.) in the turbidity data are not shown for scale matters. VCDT09 and temperature data from VCDT10 are from Berndt et al. (2016), all other parameters were acquired in this study.

An indication for the presence of hydrothermal fluids in pore waters in the vicinity of the hydrothermal vent field is found at about 4 m depth in core GC09. Here, positive Li and negative Mg concentrations (Fig. 4a) are probably caused by the weak admixing of hydrothermal solutions (Gieskes et al., 1982; Hensen et al., 2007). Likewise, $^{87}Sr/^{86}Sr$ isotope ratios decrease to a value of 0.708949 (Fig. 5) and thus tend towards the $^{87}Sr/^{86}Sr$ ratio of the local hydrothermal endmember ($^{87}Sr/^{86}Sr = 0.7052$; Von Damm, 1990). Hydrothermal endmember Li concentrations in the Guaymas Basin have been reported in a range between 630 and 1076 µM (Von Damm et al., 1985) and are 20 to 30× higher than those measured at the Smoker Site (∼ 34 µM; Fig. 4a, Table S1). Here, hydrothermal fluids account for about 3 % of the mix with seawater (Fig. 7). The sediments in this core section also change from diatomaceous clay to unconsolidated, coarse-grained hydrothermal deposits (Fe-rich sulfides; see also Sect. 3.3), which may facilitate the circulation of hydrothermal fluids.

Despite the proximity of the remaining GCs and MUCs to the hydrothermal vent field (∼ 500 m distance; temperatures immediately after retrieval are up to 60 °C) typical pore fluid indicators such as Mg, Li, and $^{87}Sr/^{86}Sr$ do not show major excursions from seawater values (Fig. 4). Similarly, NH_4, an indicator for a diagenetic or catagenetic breakdown of organic matter, is only poorly enriched in sediments surrounding the hydrothermal vents ($NH_4 \leq 0.3$ mM). NH_4 remains well below the value reported from the southern trough (20 mM; Von Damm et al., 1985) and the Slope Site (GC07) where 10 mM were already reached at subsurface depths of only a few meters (Fig. 4). The pore fluid geochemistry around the hydrothermal vent field therefore confirms that early diagenetic processes are not intense (Fig. 7) and that the shallow sediments are not significantly affected by hydrothermal fluids. We hypothesize that hydrothermal venting causes a shallow convection cell drawing seawater through the sediments towards the hydrothermal vent field, while the sediments become heated by lateral heat conduction (cf. Gamo et al., 1991; Henry et al., 1996; Kinoshita and Yamano, 1997).

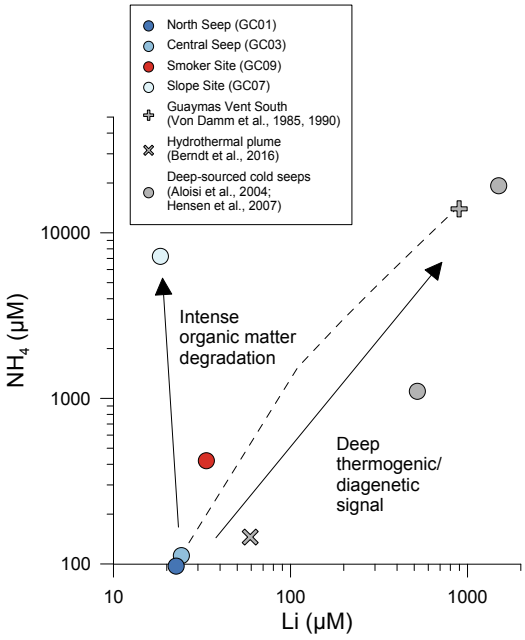

Figure 7. NH_4 (µM) versus Li concentrations (µM) of Guaymas Basin cold seeps (North, Central) and the Smoker Site. Deep fluids from the Smoker Site (GC09) mix with hydrothermal fluids with a share of ∼ 3 %. The mixing line has been calculated as follows;

$$x_{mix} = x_{phase1} \times f_1 + x_{phase2} \times f_2, \quad \text{(R1)}$$

with $f_1 + f_2 = 1$. Endmember 1 is the Guaymas Vent South (Von Damm, 1990; Von Damm et al., 1985) and endmember 2 is Guaymas North Seep. For comparison, Guaymas hydrothermal endmember fluid composition (Von Damm, 1990; Von Damm et al., 1985), hydrothermal plume fluid composition (Berndt et al., 2016), Guaymas slope sediments (GC07), and deep-sourced cold seeps (Aloisi et al., 2004; Hensen et al., 2007) are shown.

The diatomaceous clay might act as a seal to fluids migrating upwards, which are channeled to the catchment area of the rising hydrothermal fluids of the hydrothermal vent

field (see also Fig. 4 in Berndt et al., 2016). The geochemical composition of these fluids is likely influenced by a high temperature-chemical alteration of the sediment caused by the intruded sills (Fig. 2b). However, shallower pore fluids of surface sediments at the Smoker Site (i.e., 0–4 m) are not affected much by contributions from these fluids and show predominantly ambient diagenetic fluid signatures.

4.1.2 Cold seeps

The selection of sampling sites at presumed seep locations was based on existing published data (Lizarralde et al., 2010) and information from seismic records (Fig. 2). Seismic amplitude blanking along vertical zones below the seafloor indicates active fluid and/ or gas conduits at the North and Central seeps. Given that sill intrusions and related high-temperature alteration of sediments are driving the seepage, the expectation was to find deeply sourced (average sill depth ~ 400 m) fluids with a typical geochemical signature analogous to findings at hydrothermal vents in the Guaymas Basin (Von Damm et al., 1985; Von Damm, 1990; Berndt et al., 2016). Such characteristics are, e.g., a high concentration of thermogenic hydrocarbon gases formed by organic-matter degradation, enrichments in NH_4, a depletion in Mg, and a strong enrichment in fluid-mobile tracers like Li and B (e.g., Aloisi et al., 2004; Scholz et al., 2009). The hydrocarbon formation caused by abiogenic processes plays only a minor role in the hydrothermal vent field (McDermott et al., 2015; discussion in Berndt et al., 2016).

Samples obtained using a video-guided MUC revealed the highest methane concentrations at the North, Central, and Ring seeps (Fig. 4b). In conjunction with visual evidence (abundant chemosynthetic biological communities), this confirms that we have hit active seepage areas during our sampling campaign. At the two most active sites, North and Central, high methane levels are accompanied by a significant drop in sulfate and an increase in TA and TH_2S, providing evidence for AOM, according to the following net reaction;

$$CH_4 + SO_4^{2-} \rightarrow HCO_3^- + HS^- + H_2O \quad \text{(R2)}$$

(e.g., Nauhaus et al., 2005; see Wegener et al., 2016 for a recent update).

These pore-water trends are even more pronounced in GC01 (North) where the AOM zone was completely penetrated and gas hydrate was found at about 2.5 m b.s.f. Unfortunately, GCs from similarly active sites could not be obtained from the Central and Ring seeps, mainly because of patchiness of seepage spots and the widespread authigenic mineralizations at the seafloor preventing sufficient penetration. Nevertheless, active methane seepage at all three investigated sites is evident. The methane flux is, however, not accompanied by any significant excursion of pore-water constituents typical for deeply sourced, high-temperature sediment–water interactions (e.g., Mg, Cl, Li). Also, Sr concentrations show seawater values at all seep sites (Fig. 5), except for the North Seep, where values drop together with Ca due to co-precipitation during carbonate formation. The $^{87}Sr / ^{86}Sr$ ratios show predominantly seawater signatures as well (Fig. 5, Table S2). Similarly, low NH_4 concentrations of < 1 mM indicate a low intensity of organic matter decomposition (as discussed in Sect. 4.1.1). Taken together, our data show that, with the exception of methane and sulfate, the pore water corresponds to ambient diagenetic conditions that are typically met in this shallow subsurface depth. An explanation for the decoupling of methane levels and pore-water composition is that only methane is rising to the seafloor as a free gas. This assumption requires a closer look at the composition of dissolved hydrocarbons in general, which is given below.

4.2 Origin of hydrocarbon gases

4.2.1 Alteration effects

The origin of hydrocarbon gases can be deciphered by plotting $CH_4 / (C_2H_6 + C_3H_8)$ ratios versus $\delta^{13}C_{CH_4}$ data in a modified Bernard diagram (Schmidt et al., 2005 and literature therein) (Fig. 8a) and $\delta^{13}C_{CH_4}$ versus δD_{CH_4} after Whiticar (1999) and Welhan (1988) (Fig. 8b). Most of the measured stable isotope data of pore-water methane indicate a microbial origin or a mixed microbial and thermogenic origin (Fig. 8). By contrast, hydrocarbons venting at the hydrothermal vent field reflect a mixture of thermogenic methane and abiogenic methane derived from water–rock interactions (Berndt et al., 2016).

It has to be considered though that, except of three samples from the North Seep, all $\delta^{13}C_{CH_4}$ measurements were performed on samples located above the AOM zone (see Fig. 4). This implies that the upward-rising methane has likely undergone fractionation due to methane oxidation by sulfate in the AOM zone underneath. AOM enriches DIC in ^{12}C and results in progressively increasing $\delta^{13}C_{CH_4}$ values in the residual methane (Whiticar, 1999). Considering the $\delta^{13}C_{CH_4}$ at the Slope Site as a microbial endmember composition for the Guaymas Basin (Fig. 8a), most of the data fall on calculated fractionation lines for AOM, following a Rayleigh trend (Whiticar, 1999). Methane sampled close to the Smoker Site (MUC15) is obviously also affected by AOM (Fig. 8a). This is in line with recent studies on hydrothermal sediments of the southern trough of the Guaymas Basin, where bacterial and archaeal communities catalyze the oxidation of methane and higher hydrocarbons, shifting $\delta^{13}C_{CH_4}$ values to heavier signatures (Dowell et al., 2016).

The origin of methane and oxidation effects can further be identified in the $\delta^{13}C_{CH_4}$ versus δD_{CH_4} plot after Whiticar (1999) and Welhan (1988) (Fig. 8b). Slope Site samples plot in the field of microbial CO_2 reduction while hydrothermal plume samples plot in the thermogenic field. One sample even points to a mantle signature and thus shows potential endmember isotope signatures (Berndt et al., 2016).

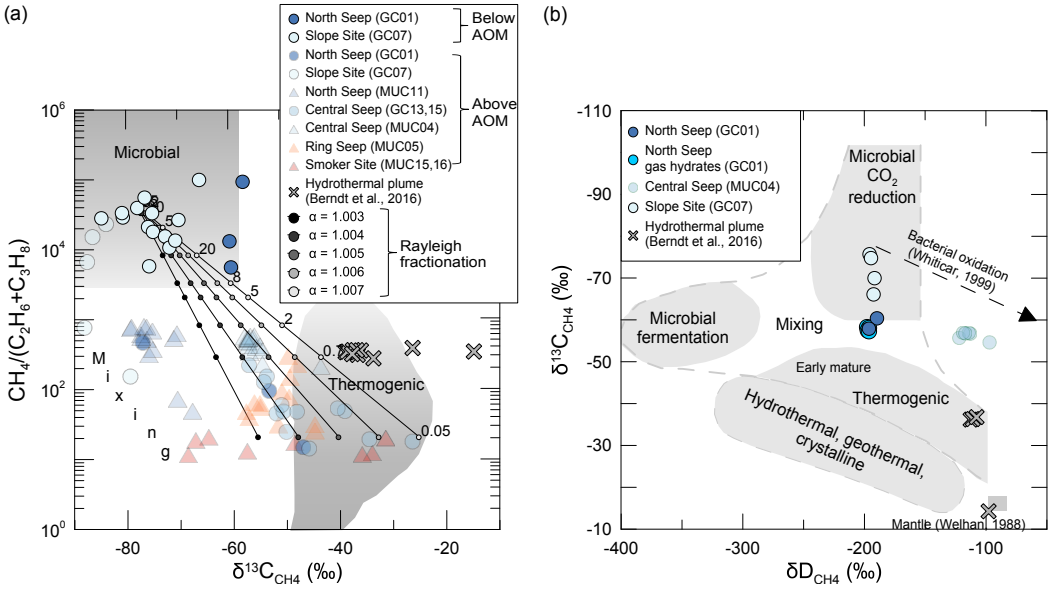

Figure 8. Hydrocarbon, $\delta^{13}C_{CH_4}$, and δD isotope data for Guaymas Basin seep sites and Smoker and Slope sites. Hydrothermal plume data are shown for comparison. Note that hydrocarbon and $\delta^{13}C_{CH_4}$ data are from Berndt et al. (2016). **(a)** $CH_4 / (C_2H_6 + C_3H_8)$ ratios versus $\delta^{13}C_{CH_4}$ data are shown after a modified Bernard diagram (Schmidt et al., 2005). Pale symbols indicate samples above the AOM zone. Rayleigh fractionation lines show the effect of (microbial) methane oxidation, and labels indicate the residual methane in %. **(b)** Carbon ($\delta^{13}C_{CH_4}$) and hydrogen (δD_{CH_4}) isotope data after Whiticar (1999) and (Welhan, 1988). Pale symbols (Central Seep – MUC04) indicate samples above AOM zone.

North Seep samples (pore fluids and gas hydrates) plot in the mixing region while samples from the Central Seep clearly shift away from the microbial field and are considered to be affected by bacterial oxidation (Whiticar, 1999).

Considering the methane below the AOM as being unaltered, three North Seep samples and the majority of the Slope Site samples show a clear microbial source of methane (Fig. 8a). All other samples appear to be affected by major oxidation following a Rayleigh fractionation process and show that only a fraction between 2 % (MUC04, Central Seep) and 0.05 % (GC15, Central Seep) remains as unoxidized methane (Fig. 8a).

4.2.2 Origin of unaltered samples

The $\delta^{13}C_{CH_4}$ versus δD_{CH_4} plot of the unaltered North Seep samples suggests a mixing of microbial and thermogenic methane (Fig. 8b). Similar signals have also been observed at Hydrate Ridge (Milkov et al., 2005) and seem to be a common phenomenon in hydrothermal and cold-seep-affected sediments. In a few samples from the North and Central seeps ethane concentrations have been high enough to measure stable carbon isotopes, and the $\delta^{13}C_{C_2H_6}$ values point to a thermogenic origin (Table S3).

4.3 Timing of active (thermogenic) methane release

4.3.1 Seep site geochemistry

Based on our data set, no deep-sourced fluid is currently migrating upwards at the cold seeps investigated (compare deep-sourced seepage sites from the Gulf of Cadiz in Fig. 7). Hence, in terms of the original hypothesis that fluid emanation is directly linked to recent sill intrusions, these cold seep sites cannot be considered active as claimed by Lizarralde et al. (2010). These authors argued that thermogenic carbon is currently released up to 50 km away from the rift axis, causing a maximum carbon flux of 240 kt C yr^{-1}. Further, Lizarralde et al. (2010) showed temperature anomalies, high methane concentrations, and helium isotopic anomalies in the water column potentially indicative of a magmatic source. These anomalies were detected in close vicinity to bacterial mats, tubeworms, and authigenic carbonates, situated above areas of sill intrusions. Comparable structures have been identified in this study by video-guided MUCs and seismic data (Fig. 2). Our detailed results on pore fluid, water column, and gas geochemistry now show that most methane was of microbial origin (Fig. 8) and only traces of thermogenic methane were found up to $\sim$ 20 km off axis (North Seep). Even pore fluids taken close to the hydrothermal vent field are dominated by shallow microbial degradation processes, indicating that the hydrothermal fluid

flow in the Guaymas Basin is rather localized and bound to focused fluid pathways. The temperature and chemical anomalies detected by Lizarralde et al. (2010) might also arise from the deep water layer in the Guaymas Basin itself, which is influenced by hydrothermal fluids (Campbell and Gieskes, 1984). Hydrothermal activity in the Guaymas Basin produces hydrothermal plumes, rise 100–300 m above seafloor and spread out along density gradients throughout the basin (Campbell and Gieskes, 1984). Our results nevertheless show that the Guaymas Basin has a well-mixed bottom seawater layer, with temperatures ranging between 2.8 and 3.9 °C in > 1000 m depth and off-axis methane concentrations that vary quite considerably (e.g., 6 to 28 nM at Ring Seep, Fig. 9). These bottom seawater variabilities are bigger than the reported anomalies by Lizarralde et al. (2010) and might indicate that thermogenic methane release might not be as widespread as previously suspected.

Pore fluids taken in a transect up to ∼ 30 km away from the rift axis show no evidence for high-T reactions (Figs. 4, 7). We can still not exclude the possibility that thermogenic methane is released in other areas of the basin, but the lack of evidence for high temperature geochemical processes at our sites is evident and clearly contradicts the conclusions drawn by Lizarralde et al. (2010). Our findings suggest that a projection of the thermogenic methane release based on the number of detected sills (Lizarralde et al., 2010) represents a maximum estimate, as it neither considers the time of the emplacement of a sill nor the lifetime of such magmatic systems. Today, shallow microbial degradation processes determine pore fluid signatures (Figs. 4, 8). Whereas high temperature thermogenic reactions have certainly been active during sill emplacement and once released large amounts of carbon, these processes have apparently ceased. However, pipe structures may still act as high-permeability pathways and facilitate the advection of gas. As a result, small amounts of thermogenic carbon might be released as reflected by the signatures of $\delta^{13}C_{CH_4}$ and the thermogenic $\delta^{13}C_{C_2H_6}$ isotope data at the North and Central seeps. However, present methane advection rates are slow (probably < 1 cm yr^{-1}), as observed by low methane gradients in the pore fluid profiles (Fig. 4). These conditions favor an effective turnover of CH_4 to bicarbonate and authigenic carbonates by AOM (Wallmann et al., 2006; Karaca et al., 2010).

4.3.2 Origin of the authigenic carbonate

The porous authigenic carbonate block recovered from the seafloor at the Central Seep can preserve long-term information about seepage in this area. The predominant biomarkers found in the seep carbonate from the Central Site (56-VgHG-4) are consistent with microbial consortia performing AOM. In particular, high abundances of crocetane and *sn*2-hydroxyarchaeol indicate major contributions from the methanotrophic archaea of the ANME-2 cluster, whereas DAGE originate from syntrophic sulfate-reducing bacteria,

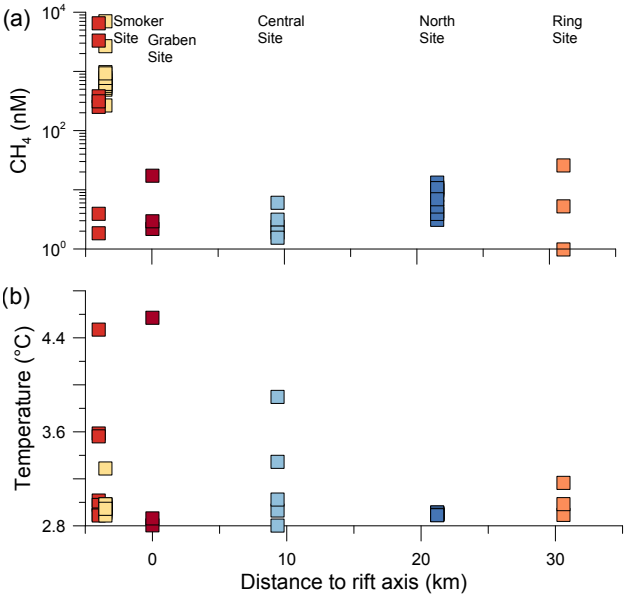

Figure 9. Water column CH_4 **(a)** and temperature **(b)** at cold seeps as well as the Smoker and Graben sites relative to the rift axis.

probably of the *Desulfosarcina–Desulfococcus* group (Blumenberg et al., 2004; Niemann and Elvert, 2008). These consortia gain energy from AOM, with sulfate as the final electron acceptor (see Eq. 2).

At the Central Seep, the increase in TA due to the AOM reaction plausibly explains the precipitation of isotopically depleted authigenic carbonates. Particularly, ANME-2 biomarkers have been reported in association with abundant fibrous, often botryoidal aragonite cements (Leefmann et al., 2008), which is in line with the observations made at the Central Seep (see Sect. 3.3). Moreover, the high abundance of ANME-2 indicates that seep carbonate formation took place under high sulfate concentrations and strong advective methane flow, but there were no elevated water temperatures (c.f. Nauhaus et al., 2005; Peckmann et al., 2009; Timmers et al., 2015). Minor amounts of typical marine sterols also show that the seep carbonates also captured detritus from the surrounding sediment and water column during their ongoing cementation.

The bulk carbonate carbon isotope signature ($\delta^{13}C_{V\text{-}PDB} = -46.6$ ‰) overlaps with the shallow, heavy $\delta^{13}C_{CH_4}$ values (−27.5 ‰ and −48.6 ‰) in the pore fluids at the Central Seep and confirms a dominant AOM signature with a minor planktonic and potentially $\delta^{13}C$-diluting background signal. The oxygen isotopes point to a low formation temperature of about 3 °C, consistent with a precipitation in bottom waters (2.8 to 3.0 °C (Figs. 6, 9; Table S4). The $^{87}Sr/^{86}Sr$ analyses support this assumption by values within uncertainty identical to modern seawater. U-Th carbonate dating provide ages younger than 240 yrs BP. In summary, authigenic carbon-

ates originate from shallow methane and were subrecently formed in ambient seawater.

4.3.3 Timing of off-axis hydrothermal activity

The seismic data taken across the seep locations indicate that the disrupted sediment layers do not reach the sediment surface (Fig. 2a, c). This implies that fluid mobilization ceased at some time before the uppermost sediment layers were deposited. The doming above the Central Seep provides some clues on the timing of fluid migration (Fig. 2c). Assuming that the doming is the result of buoyancy-related uplift (Koch et al., 2015), it represents the time when intrusion-related gas reached the seafloor. Assuming further a sedimentation rate of 1.7 m per 1000 years (Central Seep; Table 1) and maxima and minima deposition depths of 48 and 12 m below seafloor, respectively (see Fig. 2c), this would imply that most of the gas reached the seafloor between 28 and 7 kyr ago. Even at maxima and minima sedimentation rates of 3.5 m (North Seep) and 0.5 m (Ring Seep) per 1000 years, the gas flow would have ceased between 14 and 3 kyr ago at the earliest and between 96 and 24 kyr ago at the latest. Accordingly, this finding further supports the results of the pore fluid and gas geochemistry, which show no sign of active fluid flow from a depth at the cold seep sites in the northern Guaymas Basin.

We agree with Lizarralde et al. (2010) that hydrothermal activity in the Guaymas Basin is an important driver for CH_4 (and CO_2) emissions into bottom waters. However, our data set shows that there is no deep fluid advection at the investigated sites. Our interpretation is that hydrothermal activity at these off-axis locations has ceased and previously formed pathways seem to mediate the advection of biogenic gas at present. It is not unlikely that seep-induced, hydrothermal activity is still ongoing in other places than those investigated in this study, but in order to provide more accurate predictions for (thermogenic) carbon fluxes and the potential impact on the climate, sill emplacement mechanisms need to be better constrained. Apart from their spatial distribution, the most important and currently unknown factors are the determination of the time of their emplacement and the longevity of the sill-systems that require further investigation.

5 Conclusions

Magmatic sill intrusions into organic-rich sediments can potentially release large amounts of carbon into the water column and atmosphere and are therefore considered potential trigger mechanisms for rapid climate change, e.g., during the PETM. Sill-induced hydrothermalism has been reported along the ridge axis in the Guaymas Basin (von Damm et al., 1985; Berndt et al., 2016) and the widespread occurrence of sills and fluid escape features within the basin has been used to estimate the related carbon release (Lizarralde et al., 2010). Our investigations of off-axis methane seeps in the Guaymas Basin demonstrate that there are no indications for hydrothermal activity away from ridge axis at present. These conclusions are mainly based on the lack of geochemical signals from high temperature alteration processes and the CH_4 predominantly originating from microbial degradation. We suggest that hydrothermal circulation has, based on seismic records and dating of authigenic carbonates, largely ceased at the investigated sites several thousands of years ago. This finding underlines that the vigorous venting, as presently observed at the ridge axis, is a very effective way to release sedimentary carbon into the water column but must be considered a very short-lived process in a geological sense. Hence, a more comprehensive understanding of these hydrothermal systems with respect to their climatic relevance requires a better knowledge of the control mechanisms and their longevity.

Data availability. All research data is accessible in the supplement of this manuscript.

The Supplement related to this article is available online at https://doi.org/10.5194/bg-15-5715-2018-supplement.

Author contributions. SG, CH, MS, VL, FS, and AF were involved in research cruise SO241 and carried out sampling, sample preparation, and measurements. MD conducted temperature measurements. ML took samples for Pb measurements, LD processed the samples, and CCS performed the analyses. SS carried out the stable hydrogen isotope measurements. VT performed the biomarker analyses. SS and CB were responsible for the seismic data recording. All authors discussed the results and commented on the manuscript. CH and CB planned the study and were responsible for the planning of the research cruise.

Competing interests. The authors declare that they have no conflict of interest.

Acknowledgements. This work was undertaken within the MAKS project funded by the German Ministry of Science and Education (BMBF). We thank the master and crew of the R/V *Sonne* for their support during the SO241 cruise. Further thanks goes to Regina Surberg, Bettina Domeyer, and Anke Bleyer for analytical support during the cruise and on shore. We greatly appreciate the support from Ana Kolevica, Tyler Goepfert, Sebastian Fessler, Andrea Bodenbinder, Yan Shen, and Jutta Heinze for onshore analyses. Additional support of this work was provided by EU-COST Action ES1301 "FLOWS" (https://www.flows-cost.eu, last access: 25 September 2018). We would also like to thank the editor Helge Niemann and two anonymous reviewers for their comments and constructive reviews.

The article processing charges for this open-access publication were covered by a Research Centre of the Helmholtz Association.

Edited by: Helge Niemann
Reviewed by: two anonymous referees

References

Aarnes, I., Svensen, H., Connolly, J. A. D., and Podladchikov, Y. Y.: How contact metamorphism can trigger global climate changes: Modeling gas generation around igneous sills in sedimentary basins, Geochim. Cosmochim. Ac., 74, 7179–7195, https://doi.org/10.1016/j.gca.2010.09.011, 2010.

Aloisi, G., Drews, M., Wallmann, K., and Bohrmann, G.: Fluid expulsion from the Dvurechenskii mud volcano (Black Sea). Part I. Fluid sources and relevance to Li, B, Sr, I and dissolved inorganic nitrogen cycles, Earth Planet. Sc. Lett., 225, 347–363, https://doi.org/10.1016/j.epsl.2004.07.006, 2004.

Bani-Hassan, N.: Numerical modeling of submarine hydrothermal fluid flow, Dr. Diss., Christian-Albrechts-Universität Kiel, Germany, 2012.

Berndt, C., Hensen, C., Mortera-Gutierrez, C., Sarkar, S., Geilert, S., Schmidt, M., Liebetrau, V., Kipfer, R., Scholz, F., Doll, M., Muff, S., Karstens, J., Planke, S., Petersen, S., Böttner, C., Chi, W.-C., Moser, M., Behrendt, R., Fiskal, A., Lever, M. A., Su, C.-C., Deng, L., Brennwald, M. S., and Lizarralde, D.: Rifting under steam – how rift magmatism triggers methane venting from sedimentary basins, Geology, 44, 767–770, 2016.

Biddle, J. F., Cardman, Z., Mendlovitz, H., Albert, D. B., Lloyd, K. G., Boetius, A., and Teske, A.: Anaerobic oxidation of methane at different temperature regimes in Guaymas Basin hydrothermal sediments, ISME J., 6, 1018–1031, https://doi.org/10.1038/ismej.2011.164, 2012.

Blumenberg, M., Seifert, R., Reitner, J., Pape, T., and Michaelis, W.: Membrane lipid patterns typify distinct anaerobic methanotrophic consortia, P. Natl. Acad. Sci. USA, 101, 11111–11116, 2004.

Calvert, S. E.: Accumulation of Diatomaceous Silica in the Sediments of the Gulf of California, Geol. Soc. Am. B., 77, 569–596, 1966.

Campbell, A. C. and Gieskes, J. M.: Water column anomalies associated with hydrothermal activity in the Guaymas Basin, Gulf of California Andrew C. Campbell and Joris M. Gieskes, Earth Planet. Sc. Lett., 68, 57–72, 1984.

Curray, J. R., Moore, D. G., Aguayo, J. E., Aubry, M.-P., Einsele, G., Fornari, D., Gieskes, J., Guerrero-Garcia, J., Kastner, M., Kelts, K., Lyle, M., Matoba, Y., Molina-Cruz, A., Niemitz, J., Rueda-Gaxiola, J., Saunders, A., Schrader, H., Simoneit, B. R. T., and Vacquier, V.,: Initial Reports of the Deep Sea Drilling Project, vol. 64., U.S. Govt. Printing Office, Washington, 1982.

DeMaster, D.: The supply and accumulation of silica in the marine environment, Geochim. Cosmochim. Ac., 5, 1715–1732, 1981.

Dickens, G. R.: Rethinking the global carbon cycle with a large, dynamic and microbially mediated gas hydrate capacitor, Earth Planet. Sc. Lett., 213, 169–183, https://doi.org/10.1016/S0012-821X(03)00325-X, 2003.

Dowell, F., Cardman, Z., Dasarathy, S., Kellermann, M. Y., Lipp, J. S., Ruff, S. E., Biddle, J. F., McKay, L. J., MacGregor, B. J., Lloyd, K. G., Albert, D. B., Mendlovitz, H., Hinrichs, K. U., and Teske, A.: Microbial communities in methane- and short chain alkane-rich hydrothermal sediments of Guaymas Basin, Front. Microbiol., 7, 17, https://doi.org/10.3389/fmicb.2016.00017, 2016.

Einsele, G., Gieskes, J. M., Curray, J., Moore, D. M., Aguayo, E., Aubry, M.-P., Fornari, D., Guerrero, J., Kastner, M., Kelts, K., Lyle, M., Matoba, Y., Molina-Cruz, A., Niemitz, J., Rueda, J., Saunders, A., Schrader, H., Simoneit, B., and Vacquier, V.: Intrusion of basaltic sills into highly porous sediments, and resulting hydrothermal activity, Nature, 283, 441–445, https://doi.org/10.1017/CBO9781107415324.004, 1980.

Fisher, A. T. and Becker, K.: Heat flow, hydrothermal circulation and basalt intrusions in the Guaymas Basin, Gulf of California, Earth Planet. Sc. Lett., 103, 84–99, https://doi.org/10.1016/0012-821X(91)90152-8, 1991.

Gamo, T., Sakai, H., Kim, E.-S., Shitashima, K., and Ishibashi, J.-I.: High-alkalinity due to sulfate reduction in the CLAM hydrothermal field, Okinawa Trough, Earth Planet. Sc. Lett., 107, 328–338, 1991.

Gieskes, J. M., Kastner, M., Einsele, G., Kelts, K., and Niemitz, J.: Hydrothermal Activity in the Guaymas Basin, Gulf of California: A synthesis, in In Initial Reports of the Deep Sea Drilling Project, 64, edited by: Blakeslee, J., Platt, L. W., and Stout, L. N., 1159–1167, 1982.

Gieskes, J. M., Gamo, T., and Brumsack, H.: Chemical methods for interstitial water analysis aboard Joides Resolution, Ocean Drill. Prog. Tech. Note 15. Texas A&M Univ. Coll. Stn., 1991.

Goldsmith, J. R., Graf, D. L., and Heard, H. C.: Lattice constants of the calcium-magnesium carbonates, Am. Miner., 46, 453–457, 1961.

Grasshoff, K., Erhardt, M., and Kremling, K.: Methods of Seawater Analysis, Wiley-VCH, Weinheim, 2002.

Gutjahr, M., Ridgwell, A., Sexton, P. F., Anagnostou, E., Pearson, P. N., Pälike, H., Norris, R. D., Thomas, E., and Foster, G. L.: Very large release of mostly volcanic carbon during the Palaeocene–Eocene Thermal Maximum, Nature, 548, 573–577, https://doi.org/10.1038/nature23646, 2017.

Hartmann, A. and Villinger, H.: Inversion of marine heat flow measurements by expansion of the temperature decay function, Geophys. J. Int., 148, 628–636, https://doi.org/10.1046/j.1365-246X.2002.01600.x, 2002.

Henry, P., Le Pichon, X., Lallement, S., Lance, S., Martin, J. B., Foucher, J. P., Fiala-Médioni, A., Rostek, F., Guilhaumou, N., Pranal, V., and Castrec, M.: Fluid flow in and around a mud volcano seaward of the Barbados accretionary wedge: Results from Manon cruise, J. Geophys. Res., 101, 20297–20323, 1996.

Hensen, C., Nuzzo, M., Hornibrook, E., Pinheiro, L. M., Bock, B., Magalhães, V. H., and Brückmann, W.: Sources of mud volcano fluids in the Gulf of Cadiz-indications for hydrothermal imprint, Geochim. Cosmochim. Ac., 71, 1232–1248, https://doi.org/10.1016/j.gca.2006.11.022, 2007.

Hinrichs, K.-U., Pancost, R. D., Summons, R. E., Sprott, G. D., Sylva, S. P., Sinninghe Damsté, J. S., and Hayes, J. M.: Mass spectra of sn -2-hydroxyarchaeol, a polar lipid biomarker for anaerobic methanotrophy, Geochem. Geophy. Geosy., 1, 11–13, 2000.

Howarth, R. J. and McArthur, J. M.: Strontium isotope stratigraphy, in A Geological Time Scale, with Look-up Table Version 4, edited by: Gradstein, F. M. and Ogg, J. G., Cambridge University Press, Cambridge, U.K., 96–105, 2004.

Huh, C.-A., Su, C.-C., Wang, C.-H., Lee, S.-Y., and Lin, I.-T.: Sedimentation in the Southern Okinawa Trough – Rates, turbidites and a sediment budget, Mar. Geol., 231, 129–139, 2006.

Ivanenkov, V. N. and Lyakhin, Y. I.: Determination of total alkalinity in seawater, in In Methods of Hydrochemical Investigations in the Ocean, edited by: Bordovsky, O. K. and Ivanenkov, V. N., Nauka Publishing House, Moscow, 110–114, 1978 (in Russian).

Iyer, K., Schmid, D. W., Planke, S., and Millett, J.: Modelling hydrothermal venting in volcanic sedimentary basins: Impact on hydrocarbon maturation and paleoclimate, Earth Planet. Sc. Lett., 467, 30–42, https://doi.org/10.1016/j.epsl.2017.03.023, 2017.

Jahnke, R. A., Emerson, S. R., and Murray, J. W.: A model of oxygen reduction, denitrification, and organic matter mineralization in marine sediments, Limnol. Oceanogr., 27, 610–623, https://doi.org/10.4319/lo.1982.27.4.0610, 1982.

Karaca, D., Hensen, C., and Wallmann, K.: Controls on authigenic carbonate precipitation at cold seeps along the convergent margin off Costa Rica, Geochem. Geophy. Geosy., 11, 1–19, https://doi.org/10.1029/2010GC003062, 2010.

Kastner, M.: Evidence for Two Distinct Hydrothermal Systems in the Guaymas Basin, in: Initial Reports of the Deep Sea Drilling Project, vol. 64, Pt. 2, edited by: Blakeslee, J., Platt, L. W., and Stout, L. N., Moore, U.S. Govt. Printing Office, Washington, 1143–1157, 1982.

Kastner, M. and Siever, R.: Siliceous Sediments of the Guaymas Basin: The Effect of High Thermal Gradients on Diagenesis, J. Geol., 91, 629–641, https://doi.org/10.1086/628816, 1983.

Kinoshita, M. and Yamano, M.: Hydrothermal regime and constraints on reservoir depth of the Jade site in the Mid-Okinawa Trough inferred from heat flow measurements, J. Geophys. Res., 102, 3183–3194, 1997.

Koch, S., Berndt, C., Bialas, J., Haeckel, M., Crutchley, G., Papenberg, C., Klaeschen, D., and Greinert, J.: Gas-controlled seafloor doming, Geology, 43, 571–574, https://doi.org/10.1130/G36596.1, 2015.

Lee, S.-Y., Huh, C.-A., Su, C.-C., and You, C.-F.: Sedimentation in the Southern Okinawa Trough: enhanced particle scavenging and teleconnection between the Equatorial Pacific and western Pacific margins, Deep. Res., 51, 1769–1780, 2004.

Leefmann, T., Bauermeister, J., Kronz, A., Liebetrau, V., Reitner, J., and Thiel, V.: Miniaturized biosignature analysis reveals implications for the formation of cold seep carbonates at Hydrate Ridge (off Oregon, USA), Biogeosciences, 5, 731–738, https://doi.org/10.5194/bg-5-731-2008, 2008.

Lizarralde, D., Soule, S. A., Seewald, J. S., and Proskurowski, G.: Carbon release by off-axis magmatism in a young sedimented spreading centre, Nat. Geosci., 4, 50–54, https://doi.org/10.1038/ngeo1006, 2010.

Lonsdale, P. and Becker, K.: Hydrothermal plumes, hot springs, and conductive heat flow in the Southern Trough of Guaymas Basin, Earth Planet. Sc. Lett., 73, 211–225, https://doi.org/10.1016/0012-821X(85)90070-6, 1985.

Lupton, J. E.: Helium-3 in the Guaymas Basin: Evidence for injection of mantle volatiles in the Gulf of California, J. Geophys. Res., 84, 7446, https://doi.org/10.1029/JB084iB13p07446, 1979.

McDermott, J. M., Seewald, J. S., German, C. R., and Sylva, S. P.: Pathways for abiotic organic synthesis at submarine hydrothermal fields, P. Natl. Acad. Sci. USA, 112, 7668–7672, 2015.

Milkov, A. V., Claypool, G. E., Lee, Y. J., and Sassen, R.: Gas hydrate systems at Hydrate Ridge offshore Oregon inferred from molecular and isotopic properties of hydrate-bound and void gases, Geochim. Cosmochim. Ac., 69, 1007–1026, https://doi.org/10.1016/j.gca.2004.08.021, 2005.

Nauhaus, K., Treude, T., Boetius, A., and Krüger, M.: Environmental regulation of the anaerobic oxidation of methane: A comparison of ANME-I and ANME-II communities, Environ. Microbiol, 7, 98–106, 2005.

Niemann, H. and Elvert, M.: Diagnostic lipid biomarker and stable isotope signatures of microbial communities mediating the anaerobic oxidation of methane with sulphate, Org. Geochem., 39, 1668–1677, 2008.

Peckmann, J., Birgel, D., and Kiel, S.: Molecular fossils reveal fluid composition and flow intensity at a Cretaceous seep, Geology, 37, 847–850, 2009.

Pfender, M. and Villinger, H.: Miniaturized data loggers for deep sea sediment temperature gradient measurements, Mar. Geol., 186, 557–570, https://doi.org/10.1016/S0025-3227(02)00213-X, 2002.

Sahling, H., Rickert, D., Lee, R. W., Linke, P., and Suess, E.: Macrofaunal community structure and sulfide flux at gas hydrate deposits from the Cascadia convergent margin, NE Pacific, Mar. Ecol.-Prog. Ser., 231, 121–138, 2002.

Schmidt, M., Hensen, C., Mörz, T., Müller, C., Grevemeyer, I., Wallmann, K., Mau, S., and Kaul, N.: Methane hydrate accumulation in "Mound 11" mud volcano, Costa Rica forearc, Mar. Geol., 216, 83–100, https://doi.org/10.1016/j.margeo.2005.01.001, 2005.

Schmidt, M., Linke, P., Sommer, S., Esser, D., and Cherednichenko, S.: Natural CO2 Seeps Offshore Panarea?: A Test Site for Subsea CO2 Leak Detection Limit, Mar. Technol. Soc. J., 49, 19–30, 2015.

Scholz, F., Hensen, C., Reitz, A., Romer, R. L., Liebetrau, V., Meixner, A., Weise, S. M., and Haeckel, M.: Isotopic evidence (87Sr/86Sr, δ7Li) for alteration of the oceanic crust at deep-rooted mud volcanoes in the Gulf of Cadiz, NE Atlantic Ocean, Geochim. Cosmochim. Ac., 73, 5444–5459, https://doi.org/10.1016/j.gca.2009.06.004, 2009.

Simoneit, B. R. T., Leif, R. N., Sturz, A. A., Sturdivant, A. E., and Gieskes, J. M.: Geochemistry of shallow sediments in Guaymas Basin, gulf of California: hydrothermal gas and oil migration and effects of mineralogy, Org. Geochem., 18, 765–784, https://doi.org/10.1016/0146-6380(92)90046-Z, 1992.

Sommer, S., Linke, P., Pfannkuche, O., Schleicher, T., Deimling, J. S. V, Reitz, A., Haeckel, M., Flögel, S., and Hensen, C.: Seabed methane emissions and the habitat of frenulate tubeworms on the Captain Arutyunov mud volcano (Gulf of Cadiz), Mar. Ecol.-Prog. Ser., 382, 69–86, https://doi.org/10.3354/meps07956, 2009.

Svensen, H., Planke, S., Malthe-Sorenssen, A., Jamtveit, B., Myklebust, R., Eidem, T. R., and Rey, S. S.: Release of methane from a

volcanic basin as a mechanism for initial Eocene global warming, Nature, 429, 3–6, https://doi.org/10.1038/nature02566, 2004.

Teske, A., Callaghan, A. V., and LaRowe, D. E.: Biosphere frontiers of subsurface life in the sedimented hydrothermal system of Guaymas Basin, Front. Microbiol., 5, 1–11, https://doi.org/10.3389/fmicb.2014.00362, 2014.

Teske, A., De Beer, D., McKay, L. J., Tivey, M. K., Biddle, J. F., Hoer, D., Lloyd, K. G., Lever, M. A., Røy, H., Albert, D. B., Mendlovitz, H. P., and MacGregor, B. J.: The Guaymas Basin hiking guide to hydrothermal mounds, chimneys, and microbial mats: Complex seafloor expressions of subsurface hydrothermal circulation, Front. Microbiol., 7, 1–23, https://doi.org/10.3389/fmicb.2016.00075, 2016.

Timmers, P. H., Widjaja-Greefkes, H. A. Ramiro-Garcia, J., Plugge, C. M., and Stams, A. J.: Growth and activity of ANME clades with different sulfate and sulfide concentrations in the presence of methane, Front. Microbiol., 6, 988, https://doi.org/10.3389/fmicb.2015.00988, 2015.

Von Damm, K.: Seafloor Hydrothermal Activity: Black Smoker Chemistry And Chimneys, Annu. Rev. Earth Planet. Sc., 18, 173–204, https://doi.org/10.1146/annurev.earth.18.1.173, 1990.

Von Damm, K. L., Edmond, J. M., Measures, C. I., and Grant, B.: Chemistry of submarine hydrothermal solutions at Guaymas Basin, Gulf of California, Geochim. Cosmochim. Ac., 49, 2221–2237, 1985.

Wallmann, K., Drews, M., Aloisi, G., and Bohrmann, G.: Methane discharge into the Black Sea and the global ocean via fluid flow through submarine mud volcanoes, Earth Planet. Sc. Lett., 248, 544–559, https://doi.org/10.1016/j.epsl.2006.06.026, 2006.

Wegener, G., Krukenberg, V., Ruff, S. E., Kellermann, M. Y., and Knittel, K.: Metabolic capabilities of microorganisms involved in and associated with the anaerobic oxidation of methane, Front. Microbiol., 7, 46, https://doi.org/10.3389/fmicb.2016.00046, 2016.

Welhan, J. A.: Origins of methane in hydrothermal systems, Chem. Geol., 71, 183–198, https://doi.org/10.1016/0009-2541(88)90114-3, 1988.

Whiticar, M. J.: Carbon and hydrogen isotope systematics of bacterial formation and oxidation of methane, Chem. Geol., 161, 291–314, 1999.

Zachos, J. C., Wara, M. W., Bohaty, S., Delaney, M. L., Petrizzo, M. R., Brill, A., Bralower, T. J., and Premoli-Silva, I.: A transient rise in tropical sea surface temperature during the Paleocene-Eocene thermal maximum, Science, 302, 1551–1554, https://doi.org/10.1126/science.1090110, 2003.